Short communication

Use of strontium titanate (SrTiO$_3$) as an anode material for lithium-ion batteries

Derek C. Johnson, Amy L. Prieto *

Department of Chemistry, Colorado State University, Fort Collins, CO 80523, USA

ARTICLE INFO

ABSTRACT

Strontium titanate nanoparticles have been synthesized using a combination of sol-precipitation and hydrothermal techniques for subsequent testing as an anode material for lithium-ion batteries. The potentials associated with lithiation are 0.105 V and 0.070 V vs. Li/Li$^+$ and 0.095 V and 0.142 V vs. Li/Li$^+$ during de-lithiation. These potentials are significantly lower than the 1.0 V to 1.5 V vs. Li/Li$^+$ typically reported in the literature for titanates. In an attempt to improve the lithiation and de-lithiation kinetics, as well as capacity retention, SrTiO$_3$ nanoparticles were platinized using a photoinduced reduction of chloroplatinic acid. No significant changes in the morphology or crystal structure of the platinized nanoparticles were observed as a result of the reduction reaction. The voltage profile, charge and discharge kinetics, and cyclability of the platinized SrTiO$_3$ nanoparticles are compared to that of the non-platinized SrTiO$_3$ nanoparticles.

© 2011 Elsevier B.V. All rights reserved.

1. Introduction

With a greater consensus regarding global warming and pollution effects associated with burning carbon based fuels, the attention to reevaluate energy delivery and storage has grown [1]. All electric vehicles (EV) and plug-in hybrid electric vehicles (HEV) have attracted great interest because they have shown the ability to reduce emissions and decrease fuel consumption [2]. However, these vehicles have not been realized on a large scale and still remain a niche market because of battery performance and cost. A key challenge to achieving better performance in Li-ion batteries is increasing the charge and discharge rates of the cell [2,3]. The two main transport properties limiting these rates are the slow solid-state diffusion of Li-ions into the anode and cathode electrodes as well as the slow diffusion between the electrodes [4]. In order to mitigate the slow solid-state diffusion processes, research has been focused on reducing the two battery electrode features to the nanoscale [5]. Thus, the electrode morphologies of choice are nanoparticles and nanowires because the surface-to-volume ratios are high [1,4,5]. These nanostructured morphologies are gaining wide acceptance as both the anode and cathode in lithium-ion batteries because they have shown to increase the discharge and charge kinetics and enhance cyclability by decreasing the irreversible capacity loss typically observed with micron-sized architectures [6].

With respect to the anode, nanoscale titanates are considered a promising material and are currently being introduced commercially. The interest in lithium titanate is due to (1) the gravimetric capacity matching well with currently available cathode materials, (2) sufficient discharge kinetics for a wide range of applications, (3) good safety characteristics, and (4) a high durability, i.e. relatively negligible irreversible capacity losses are observed [7]. In addition to lithium titanate, transition metal titanates with a perovskite crystal structure have also shown promise. One such titanate that has not been previously investigated is SrTiO$_3$. Since SrTiO$_3$ is a semiconductor, the resistance arising from the low electronic conductivity and surface boundary interfaces can have a detrimental effect on performance [6]. To overcome this issue, herein we report that conducting nanoscale nodules are deposited on the SrTiO$_3$ surface through a photoinduced electrochemical reduction reaction to facilitate the transfer of electrons to and from the SrTiO$_3$ conduction band. The premise is that facile electron transfer from the conduction band to the electrode binder will dramatically improve the rate performance. It is expected that this approach will have wide applicability and could be applied to other semiconducting lithium-ion battery anode and cathode materials using non-lithiating conducting metals such as Pt, Cu, and Ni. While Pt is utilized in these experiments, it will be important to explore Cu and Ni due to the expense associated with the noble metal.

2. Experimental

2.1. Synthesis procedure

Strontium titanate nanoparticles have been synthesized using a combination of sol-precipitation and hydrothermal techniques

* Corresponding author. Tel.: +1 970 4911592; fax: +1 970 4911801.
E-mail addresses: alprieto@lamar.colostate.edu, Amy.Prieto@colostate.edu
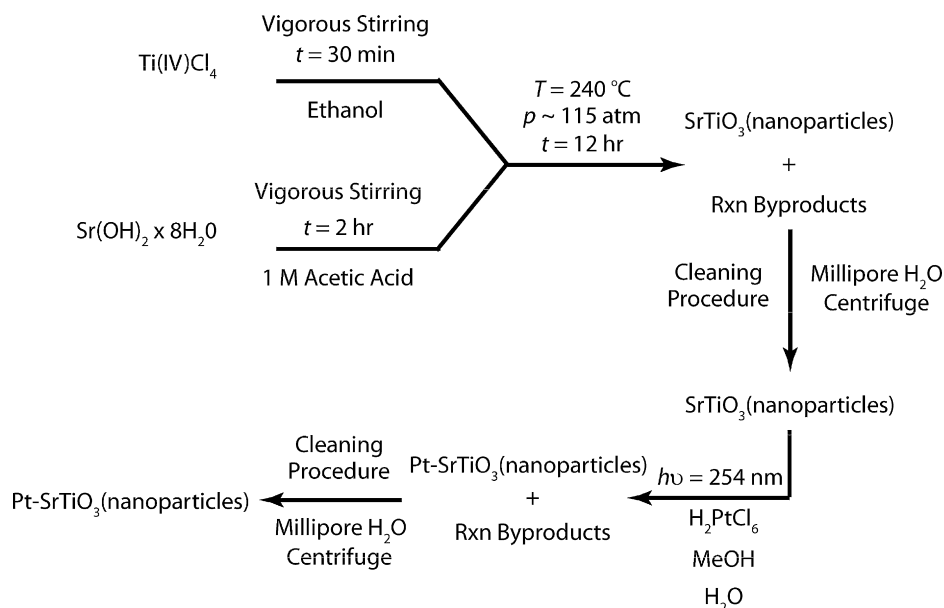(A.L. Prieto).

Fig. 1. Reaction scheme for the co-precipitation/solvothermal synthesis of SrTiO₃ nanoparticles and subsequent photoinduced reduction of chloroplatinic acid on the SrTiO₃ nanoparticle surface.

for which the reaction mechanism is contained in Fig. 1 [8]. Using standard Schlenk line techniques, two solutions, a 5% TiCl₄ (99.9%, Aldrich) in ethyl alcohol (200 proof ACS grade, Pharmco-Aaper) and a 0.2 M Sr(OH)₂·8H₂O (95%, Aldrich) in 1 M acetic acid (aq.) (ACS, Mallinckrodt chemicals), were prepared. While vigorously stirring, the solutions were combined. The resulting white slurry was transferred to a 23 mL PTFE lined acid digestion vessel (Parr, 4749). The vessel was heated at $4\,^{\circ}C\,min^{-1}$ to $240\,^{\circ}C$ and held for 12 h. The resulting product was centrifuged, decanted, and sonicated in Millipore® water at least three times to separate the nanoparticles from reaction byproducts. The nanoparticles were platinized by irradiating at 254 nm in the presence of H₂PtCl₆ (99.995%, Aldrich), methyl alcohol (99.9%, Sigma Aldrich), and Millipore® water similarly to that reported in the literature [9–11]. Reaction byproducts were removed using the same procedure as described above.

2.2. Nanoparticle characterization

The nanoparticles were characterized by transmission electron microscopy (TEM), selected-area electron diffraction (SAED), powder X-ray diffraction (XRD), and X-ray photoelectron spectroscopy (XPS). TEM images were obtained using a JEOL JEM-2000 transmission electron microscope operating under an accelerating voltage of 160 kV. Powder XRD patterns were collected on a Scintag X-2 Advanced Diffraction System equipped with Cu Kα radiation with a wavelength of 1.54 nm. XPS spectra were obtained using a Physical Electronics ESCA 5800 system employing monochromatic Al Kα ($E = 1486.6\,eV$) as the X-ray source. High resolution scans were utilized to confirm the presence and provide information regarding the bonding environment and oxidation state of Sr, Ti, O, Pt, and Cl. These scans were performed with a pass energy of 23.5 eV and a step size of $0.10\,eV\,step^{-1}$. All spectra were shifted to
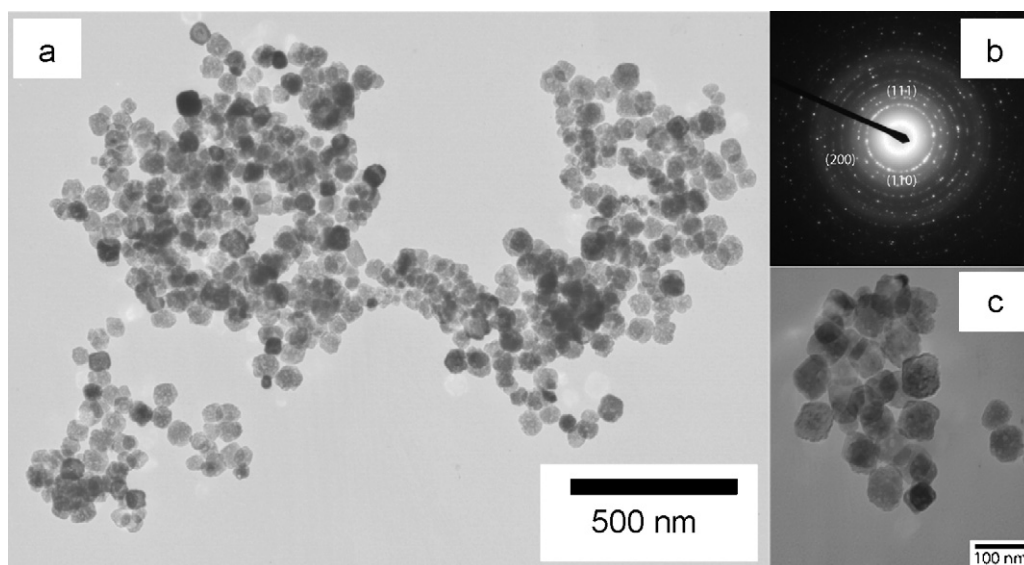

Fig. 2. (a) Characteristic TEM image of synthesized SrTiO₃ nanoparticles with (b) corresponding indexed SAED pattern. (c) Higher magnification TEM image illustrating the cubic morphology.
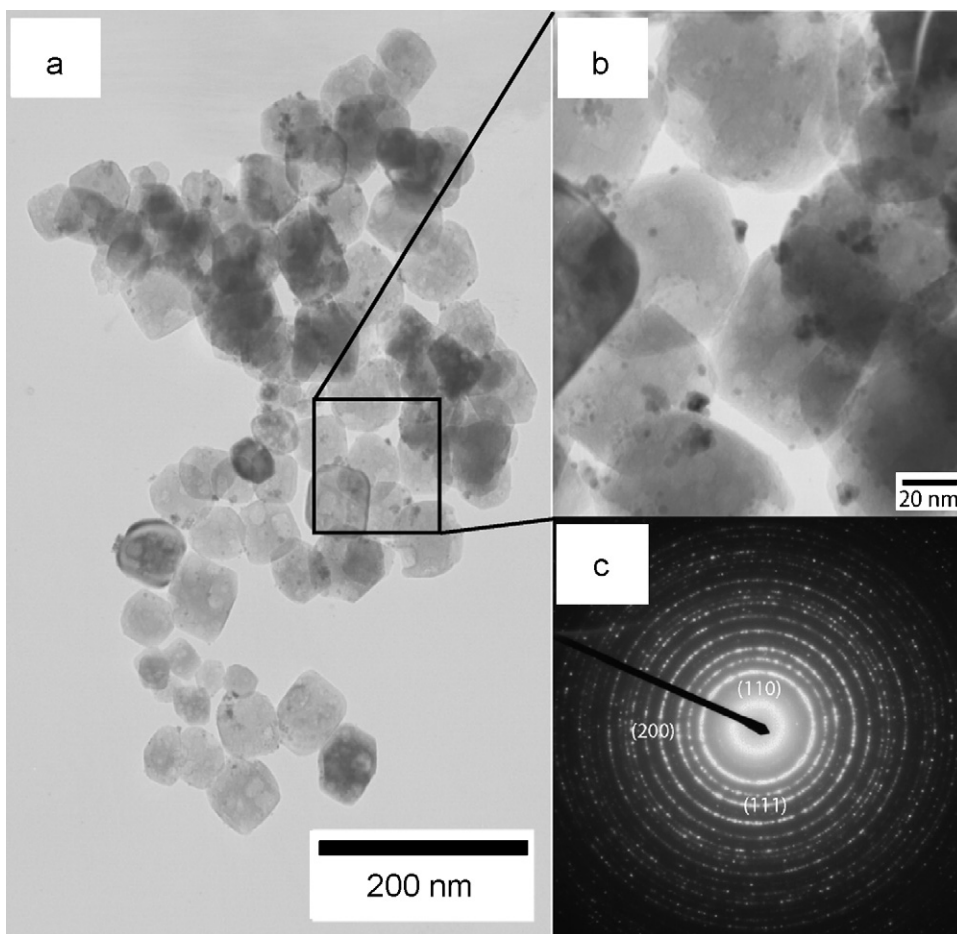
Fig. 3. (a) Characteristic TEM image of as-synthesized Pt-SrTiO$_3$ nanoparticles with (b) a high magnification TEM image illustrating Pt nodules on the surface due to the photoinduced reduction of chloroplatinic acid. (c) Corresponding indexed SAED pattern of the platinized SrTiO$_3$ nanoparticles.

account for sample charging using graphitic carbon as a reference to 284.80 eV. Preliminary cycling data was acquired using a Maccor model 4200 battery cycler in a two electrode half cell with lithium metal as the negative electrode and SrTiO$_3$ nanoparticles in a binder as the positive electrode. The positive electrode was prepared by combining 60% 1-methyl-2-pyrolidinone (99+%, Sigma–Aldrich), 28% SrTiO$_3$, 8% graphite (Fluka), and 4% poly(vinylidene fluoride) (PVDF) (Aldrich, MW = 530k) by weight. The resulting slurry was spread on copper foil and heated to 60 °C under air for 1 h and at 110 °C under vacuum for 90 min. The liquid electrolyte in all electrochemical cells consisted of 1 M LiClO$_4$ in a 1:1:1 by volume solution of dimethyl carbonate, diethyl carbonate, and ethylene carbonate. The geometric electrode surface area for all SrTiO$_3$ and Pt-SrTiO$_3$ cycling experiments was 1.27 cm^2. The platinized and non-platinized strontium titanate half cells were cycled between 0.050 V and 1.0 V vs. Li/Li$^+$ and contained an average of 0.023 g of active material. In addition, an electrode without active material, i.e. consisting of only PVDF binder and graphite, was also cycled to determine the contribution from the graphite. The geometric surface area for this cell was 0.32 cm^2 and contained 1.8 mg of graphite. The graphite cell was cycled from 2 V to 0.005 V vs. Li/Li$^+$.

3. Results and discussion

Fig. 2 contains characteristic TEM images and a SAED pattern of SrTiO$_3$ synthesized following the procedure described above. As demonstrated by Fig. 2(a), the average particle diameter is sub-100 nm. The SAED pattern contained in Fig. 2(b) was indexed to Tausonite, cubic SrTiO$_3$. All rings were indexed, but only the (1 1 0),

(1 1 1), and (2 0 0) planes are labeled for clarity. The characteristic high resolution TEM image in Fig. 2(c) visually demonstrates the cubic nature of the crystals. To determine if the platinization process affects the crystal properties or changes the particle morphology, the same characterization was performed for Pt-SrTiO$_3$ nanocrystals synthesized using the above described procedure. Fig. 3 contains characteristic TEM images and a SAED pattern of Pt-SrTiO$_3$. As illustrated in Fig. 3(a), the platinization process does not significantly alter the nanoparticle morphology as the particles are still cubic with a sub-100 nm diameter. A striking difference between the platinized and non-platinized SrTiO$_3$, highlighted by the high resolution TEM image in Fig. 3(b), is that Pt-SrTiO$_3$ contains Pt nodules on the particle surface that range in size from approximately 1 to 5 nm. As with the non-platinized particles, the SAED pattern contained in Fig. 3(c) can be indexed to tausonite, but only the (1 1 0), (1 1 1), and (2 0 0) planes are labeled for clarity. Focusing on the (1 1 1) and (2 0 0) planes, ring broadening is observed due to the presence of cubic platinum. To further confirm the purity and crystal structure of the SrTiO$_3$ as well as the presence of metallic Pt, XRD and XPS characterization techniques were used.

Fig. 4(a) and (b) contains powder XRD patterns that have been indexed to SrTiO$_3$ (PDF #00-035-0734) and Pt-SrTiO$_3$ (Pt PDF #03-065-2868), respectively. The patterns are essentially identical except for the fact that the Pt-SrTiO$_3$ pattern contains peaks at approximately 40° and 46° 2-theta that are asymmetric with shoulders at higher 2-theta. These shoulders can be attributed to the presence of the Pt nodules on the surface of the SrTiO$_3$ nanoparticles. Therefore, the *ex situ* photoinduced reduction of chloroplatinic acid does not significantly change the XRD pattern with the excep-
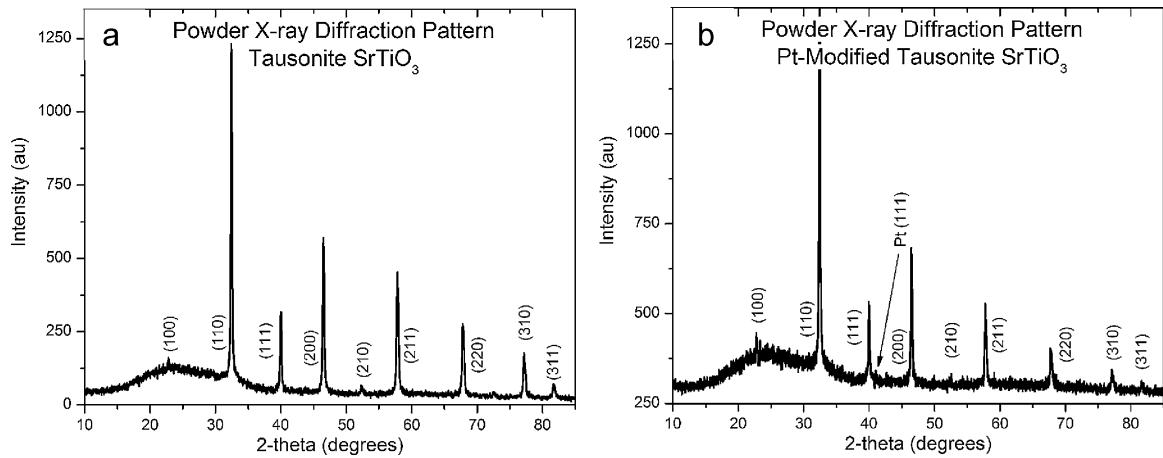
Fig. 4. Indexed powder XRD patterns for (a) SrTiO$_3$ and (b) platinized SrTiO$_3$.

tion of Pt peaks, of which the Pt(1 1 1) plane is highlighted in Fig. 4(b). A Scherrer analysis on the (1 1 0) plane suggests that the average particle diameter is approximately 100 nm. This analysis further corroborates the data and conclusions drawn from the electron microscopy characterization of the nanoparticles. To confirm that the Pt is zero valent, the chlorine byproducts were removed, and the platinization process did not affect the surface binding environment of the SrTiO$_3$, XPS analysis of the platinized and non-platinized samples were conducted.

Fig. 5(a) contains survey scans of SrTiO$_3$, chloroplatinic acid, and Pt-SrTiO$_3$. Sr, Ti, and O are identified in both the SrTiO$_3$ and Pt-SrTiO$_3$ spectra while Pt is identified in the chloroplatinic acid and Pt-SrTiO$_3$ spectra. Cl was only identified in the chloroplatinic acid survey scan. High resolution scans of Ti, Sr, O, Pt, and Cl were also collected and are plotted in Fig. 5(b)–(f), respectively, to determine the element oxidation state and changes in chemical binding environment. No observable differences in the Ti, Sr, or O XPS spectra

were detected when comparing SrTiO$_3$ and Pt-SrTiO$_3$. This suggests that neither the oxidation state nor the surface binding environment of the three elements changes as a result of the photoinduced reduction of chloroplatinic acid on the SrTiO$_3$ surface. However, high resolution spectra of Pt contained in Fig. 5(e) for both the platinized SrTiO$_3$ and chloroplatinic acid indicate that both the oxidation state and the binding environment change as a result of the photoinduced reduction of chloroplatinic acid. The top spectrum is indicative of metallic Pt while the bottom spectrum is indicative of Pt^{4+} in two different bonding environments [12]. The high resolution scan of Cl contained in Fig. 5(f) demonstrates that the chlorine byproducts have been effectively removed. Now that it has been confirmed that metallic, non-lithiating Pt has been selectively deposited onto the SrTiO$_3$ surface with the purpose of improving electronic transport properties within the binder matrix, the lithiation and rate performance of platinized and non-platinized SrTiO$_3$ are compared.
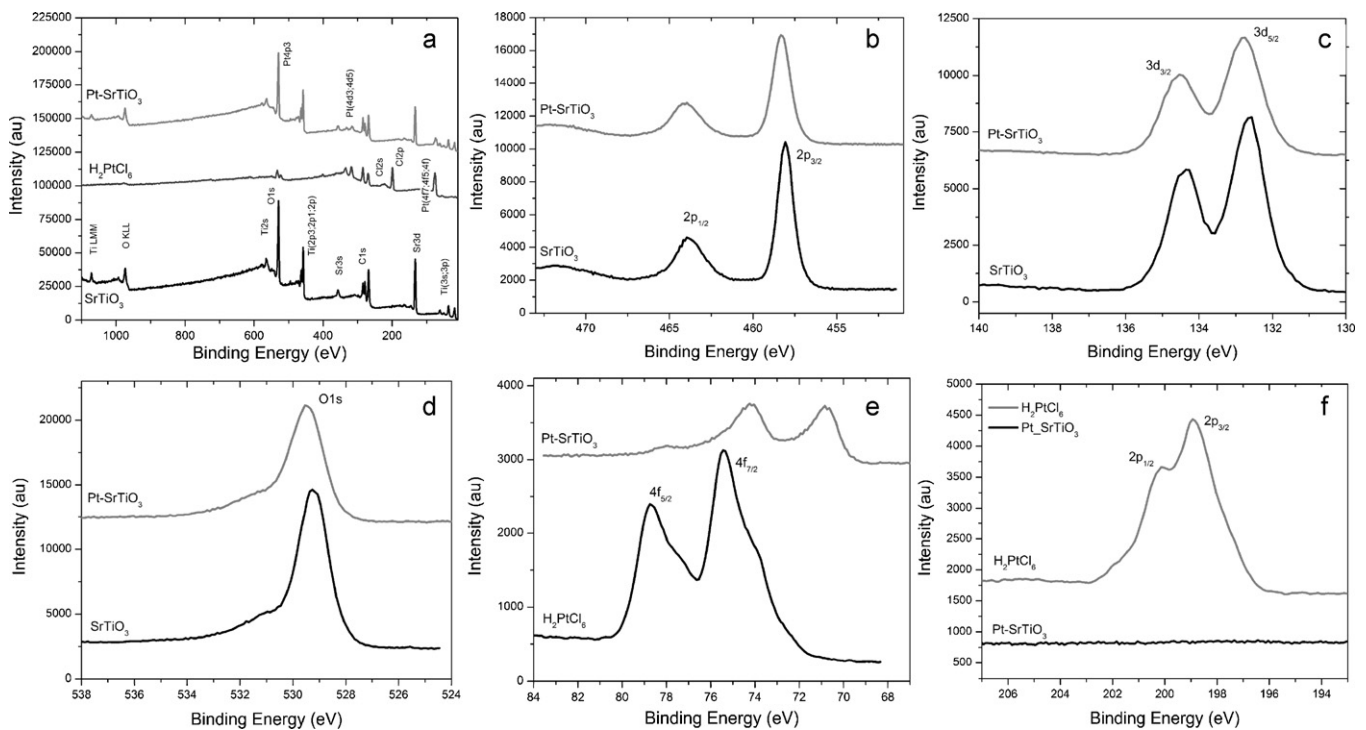

Fig. 5. (a) XPS spectra from survey scans of SrTiO$_3$, chloroplatinic acid, and Pt-SrTiO$_3$. High resolution spectra for Ti, Sr, O, Pt, and Cl are plotted in (b), (c), (d), (e), and (f), respectively.
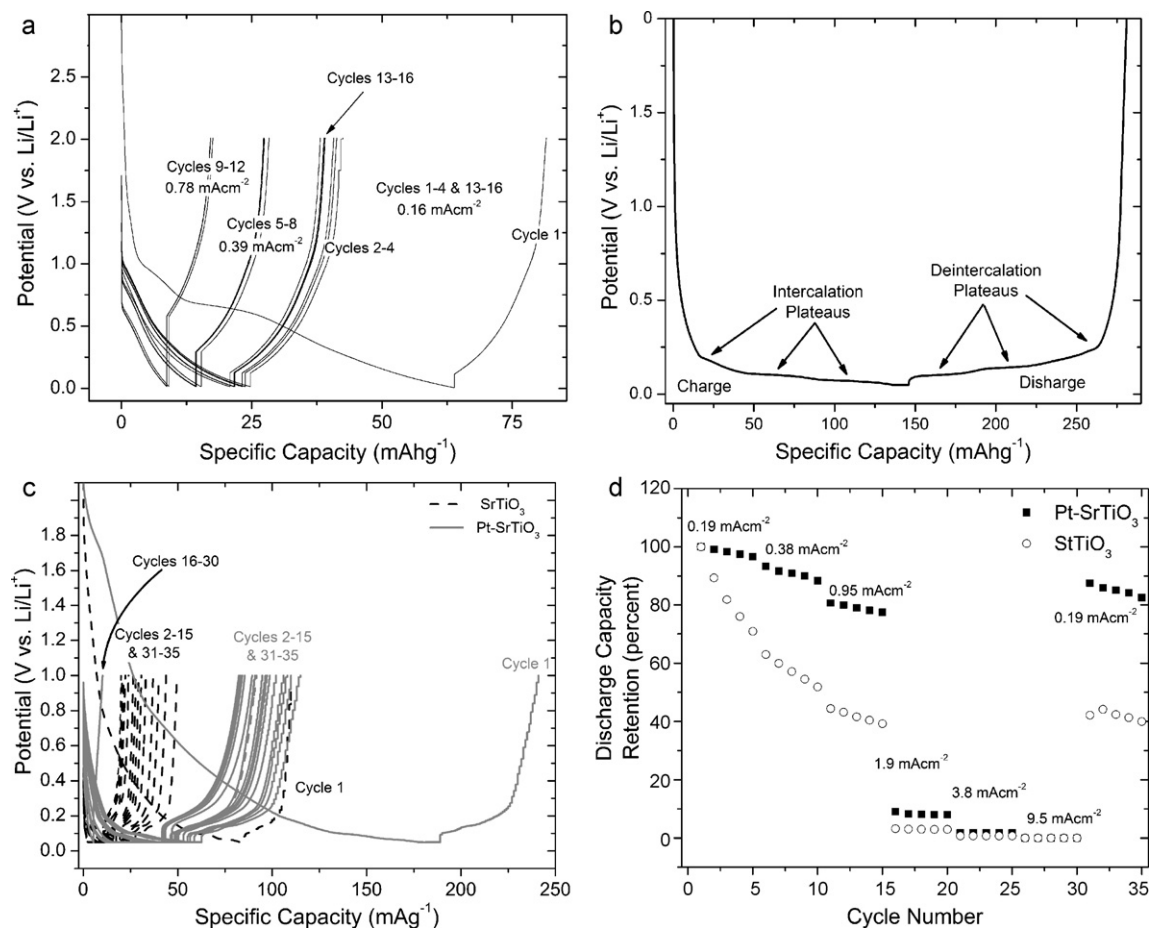
Fig. 6. (a) Charge and discharge curves of an electrode that contains only graphite and PVDF binder without anode active material. (b) A slow charge and discharge curve of $SrTiO_3$ at a rate of 0.015 mA cm^{-2} in a half cell to highlight the intercalation and deintercalation plateaus. (c) Voltage profiles of $SrTiO_3$ and Pt-$SrTiO_3$ at rates of 0.19, 0.38, and 0.95 mA cm^{-2} to highlight the difference in capacity as a function of cycle number. Cycles 16–30 for both $SrTiO_3$ and Pt-$SrTiO_3$ are not included in the plot for clarity with the exception of cycle 16 for Pt-$SrTiO_3$, which illustrates the maximum capacity of the cycles excluded from the plot. (d) A plot of the discharge capacity retention as a function of cycle number and rate for $SrTiO_3$ and Pt-$SrTiO_3$. One hundred percent discharge capacities are based on a rate of 0.19 mA cm^{-2}, and are 52.7 mAh g^{-1} and 24.8 mAh g^{-1} for Pr-$SrTiO_3$ and $SrTiO_3$, respectively.

Before the platinized and non-platinized $SrTiO_3$ samples can be compared, the effect of graphite used in the cells on the electrochemical performance must be elucidated. Voltage profiles as a function of cycle number for a cell consisting of graphite and PVDF binder are contained in Fig. 6(a). Briefly, because the graphite used as the conductive additive in the binder is not a very high grade, its capacity retention and contribution to the electrochemical properties of the cell in terms of lithium intercalation and de-intercalation is minimal. This is especially true after the first cycle and at higher charge and discharge rates. Fig. 6(b) contains a charge and discharge curve of $SrTiO_3$ highlighting two distinct and an obscure plateau for each half cycle at a rate of approximately 0.015 mA cm^{-2}. The potentials associated with the intercalation plateaus are 0.18 V, 0.105 V and 0.070 V vs. Li/Li$^+$ and 0.095 V, 0.142 V, and 0.21 vs. Li/Li$^+$ during the deintercalation of Li-ions. These potentials are significantly lower than the 1.0 V to 1.5 V vs. Li/Li$^+$ typically reported in the literature for titanates, and are positive of the potential needed to plate lithium metal. At this slow discharge rate, a capacity of approximately 135 mAh g^{-1} can be achieved. This is 87% of the theoretical capacity, 155.9 mAh g^{-1}, when two moles of lithium can be intercalated per mole of $SrTiO_3$. However, the percentage of capacity recovered when compared to the theoretical capacity quickly decreases when the cycling rate is increased. In an attempt to improve the lithiation and de-lithiation kinetics, as well as the cyclability, $SrTiO_3$ nanoparticles were platinized with a Pt loading

of less than 1% by weight using a photoinduced reduction of chloroplatinic acid. As demonstrated by Fig. 6(c), the Pt-$SrTiO_3$ retains a 2-fold higher capacity when compared to $SrTiO_3$. This trend continues for varying discharge rates as highlighted by Fig. 6(d) which contains a plot of the capacity retention as a function of discharge rate. Based on the preliminary cycling data presented in Fig. 6, it is clear that for this semiconducting material, the deposition of Pt on the $SrTiO_3$ surface helps facilitate electron transfer thereby improving the capacity retention and rate performance of this potential Li-ion battery anode material.

4. Conclusions

The photoinduced reaction of inert metals onto the surface of semiconducting, active anode materials can enhance the rate performance and capacity retention because the inert metal helps facilitate the transfer of electrons from the semiconductor to the conducting binder. Based on the potential required for lithiation, 0.105 V and 0.070 V vs. Li/Li$^+$, it is plausible that the Sr is being reduced thereby forming Li_2TiO_3 in a two step reaction process. Further experiments need to be conducted to confirm this analysis and to determine the relationship between Pt loading and the corresponding increase in rate performance and capacity retention. In addition, non-noble metals should also be explored so to not adversely affect the cost of the electrode.

Acknowledgments

References

[1] J.B. Goodenough, Y. Kim, Chem. Mater. 22 (2010) 587–603.
[2] L. Gaines, R. Cuenca, Costs of Lithium-Ion Batteries for Vehicles, Argonne National Laboratory, Department of Energy, Argonne, IL, 2000.
[3] P. Arora, Z.M. Zhang, Chem. Rev. 104 (2004) 4419–4462.
[4] B. Scrosati, J. Garche, J. Power Sources 195 (2010) 2419–2430.
[5] E. Serrano, G. Rus, J. Garcia-Martinez, Renew. Sust. Energy Rev. 13 (2009) 2373–2384.
[6] Y. Wang, H. Li, P. He, E. Hosono, H. Zhou, Nanoscale 2 (2010) 1294–1305.
[7] A.Y. Shenouda, K.R. Murali, J. Power Sources 176 (2008) 332–339.
[8] F.A. Rabuffetti, H.S. Kim, J.A. Enterkin, Y. Wang, C.H. Lanier, L.D. Marks, K.R. Poeppelmeier, P.C. Stair, Chem. Mater. 20 (2008) 5628–5635.
[9] F.B. Li, X.Z. Li, Chemosphere 48 (2002) 1103–1111.
[10] J.C. Yang, Y.C. Kim, Y.G. Shul, C.H. Shin, T.K. Lee, Appl. Surf. Sci. 121 (1997) 525–529.
[11] L. Ravichandran, K. Selvam, B. Krishnakumar, M. Swaminathan, J. Hazard. Mater. 167 (2009) 763–769.
[12] J.F. Moulder, W.F. Stickle, P.E. Sobol, K.D. Bomben, Handbook of X-ray Photo-electron Spectroscopy: A Reference Book of Standard Spectra for Identification and Interpretation of XPS Data, Physical Electronics, Eden Prairie, MN, 1995.